WOOD RESEARCH **doi.org/10.37763/wr.1336-4561/71.4.634647**
e-ISSN 2729-8906
71(4): 2026 634-647 pp.

GRAPHICAL ASSIGNMENT OF EQUIVALENT NARROW-CUT DEPTHS AND ROTATIONAL STIFFNESSES FOR FINITE-LENGTH TIE-BEAM SECTION REDUCTIONS

JÁN BRODNIANSKY, SILVIA BRODNIANSKY,
JAROSLAV SANDANUS, TOMÁŠ KLAS
SLOVAK UNIVERSITY OF TECHNOLOGY IN BRATISLAVA
SLOVAK REPUBLIC

JIŘÍ KUNECKÝ, JIŘÍ BLÁHA, MICHAL KLOIBER
CZECH ACADEMY OF SCIENCES
CZECH REPUBLIC

RECEIVED OCTOBER 2026

ABSTRACT

A graphical procedure relates finite-length tie-beam section reductions to the measured and calculated narrow-cut response of one three-frame timber roof segment. Fifteen numerical cases combine reduction lengths of 100–300 mm with remaining heights of 20–60 mm. Local displacement and midspan deflection give separate equivalent cut-depth readings; an adopted common depth is then used to read approximate rotational stiffnesses k_1 and k_2 from the adjusted measured and calculated narrow-cut series, respectively. For a 200 mm long reduction with 40 mm remaining height, the local and midspan readings are 4.89 and 5.06 cm, with an adopted depth of 5.0 cm. Agreement with the narrow-cut curves and the subsequent spring-model response are assessed separately. Both displacements yield in-range depths for 12 of the 15 cases; three exceed the calculated response range. Experimental testing covered the narrow cuts.

KEYWORDS: timber roof, cross-section reduction, equivalent narrow cut, rotational stiffness, displacement comparison.

INTRODUCTION

Assessment of historical timber roofs relies on carpentry knowledge and member/joint surveys (Yeomans 2003, Cruz et al. 2015). Roof-truss analyses address weakening and deterioration (Martinkovičová et al. 2025). OSB reinforcement can change truss flexural stiffness (Yang et al. 2020), through a mechanism distinct from ordinary roof battens. Robustness concerns the system effects of local damage (Sørensen 2011). Load transfer depends on arrangement and damage (Dietsch 2011), while redundancy can be compromised

by multiple deficient members (Munch-Andersen and Dietsch 2011). Historic roof-truss studies have examined repair techniques compatible with the original structure (Munafò et al. 2015) and modelling uncertainty in material properties and cross-sections (Zybała et al. 2022). These studies support considering local section loss within the response of the assembled structure. Timber-joint experiments and semi-rigid models describe connection flexibility (Branco and Descamps 2015, Moya and Tenorio 2017, Liu and Xiong 2018, Neusch et al. 2022, Stitic et al. 2019). Parameter identification relates model stiffness to observed responses (Lyu et al. 2017, Xiao et al. 2022). Shojo et al. (2009) represented partial sectional-area loss in wooden members by a rotational spring and examined stiffness based on affected length and flexural rigidity.

In the roof segment studied here, the intact section and an ideal hinge bound rotational restraint; an intermediate spring stiffness depends on the response and surrounding structure. A narrow saw cut concentrates the section reduction over a very short length, whereas the longer cases distribute it along a segment of the tie beam. The practical question here is whether these different geometries can be associated through the response of the same roof model. The comparison uses the displacement near the weakened region as well as the deflection of the tie-beam midspan. The former describes the local response used in the spring assignment; the latter checks the global deflection of the weakened tie beam.

The narrow-cut experiment and load redistribution were published previously (Brodniansky et al. 2026a), together with the numerical interpretation and narrow-cut spring assignments (Brodniansky et al. 2026b). The present paper develops the use of the narrow-cut response to interpret weakening distributed over a finite length. Its contribution is the graphical connection between a specified section reduction, an equivalent cut depth and an assigned rotational stiffness, accompanied by separate checks of the local and global displacements. The analysis asks how the length and remaining height affect this assignment and how closely the two displacement measures support the same replacement.

MATERIAL AND METHODS

Test specimen and numerical models

The roof segment, made of selected spruce timber, comprises three transverse frames connected by battens. Its tie beams are subjected to combined tension and bending, with interaction between frames; the specimen is not a geometrically similar replica of a specific historic roof (Tab. 1, Fig. 1). Apex straps restrain lateral movement. Concrete ballast loads all frames equally through the rafters, without contacting the battens or roof covering.

Tab. 1: Specimen, loading and model configuration.

Parameter	**Value**
Specimen	One spruce roof segment with three transverse frames
Nominal sections	Tie beams 60 × 80; rafters 40 × 60; battens 20 × 30 mm
Nominal geometry	Support-axis span 2800 mm; frame spacing 400 mm
Batten spacing	500 mm; 350 mm near the apex
Supports	Screwed wall-plate connection with flexible rotational restraint; opposite side on rollers
Ballast	Concrete blocks 400 × 400 × 50 mm; mean mass 18.2 kg; two per position, four rows on each roof side
Location of section reduction	Middle tie beam, 300 mm from the rafter-to-tie-beam connection

Parameter	Value
Measured narrow cuts	2, 4, 6 and 7 cm; fully loaded pre-cut state is measurement 19
Comparison displacements	Mean displacement of optical targets and vertical tie-beam midspan deflection
Member moduli based on bending tests	Tie beams: 10 GPa (middle/laboratory), 12 GPa (entrance); rafters: 9 GPa (laboratory roller/middle restrained sides), 14 GPa (others); battens: 15 GPa
Narrow-cut segment	Length 2 mm; eccentricities 0/10/20/30/35 mm at depths 0/2/4/6/7 cm; rigid offset links
Assigned local bilinear inputs	Bilinear nonlinear elastic: E = 10000 MPa, G = 630 MPa; tensile/compressive transitions 11/20 MPa; E_p = 4 MPa

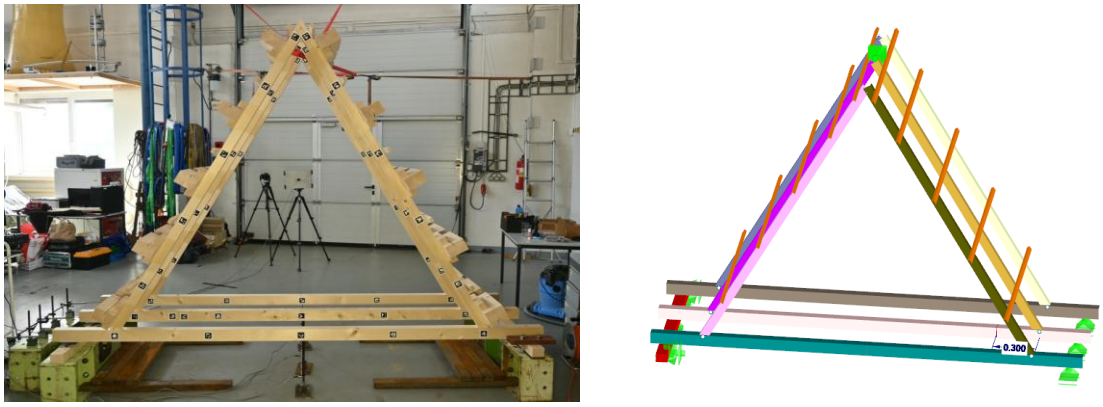


Fig. 1: Unloaded three-frame experimental roof segment (left) and its three-frame RFEM model (right).

Progressive cutting followed the fully loaded intact state: measurements 20–23 correspond to depths of 2, 4, 6 and 7 cm. Complete severing in measurement 24 is excluded from the stiffness analysis. Fig. 2 shows the deeper cut states.

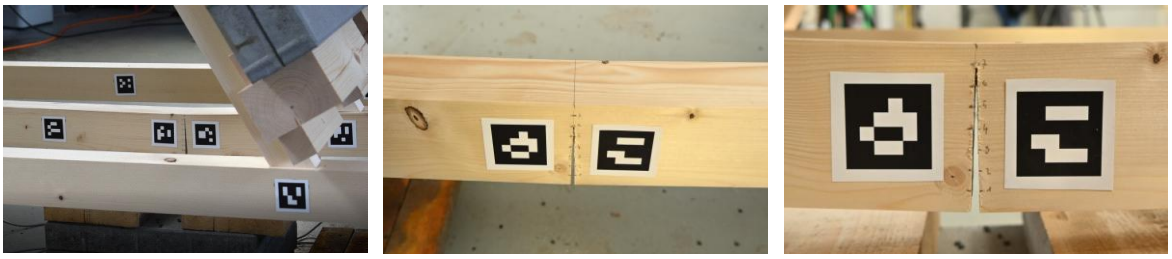


Fig. 2: Progressive cutting of the middle tie beam: cut location in the loaded specimen at the 7 cm stage (left), and cut openings at 6 cm (centre) and 7 cm (right).

The three-frame RFEM model (Fig. 1, right) uses one-dimensional beam elements with the idealizations described by Brodniansky et al. (2026b). Batten fastener slip is omitted. The member moduli in Tab. 1 were adopted from post-test static bending results for tie beams, rafters and battens (Brodniansky et al. 2026a,b). The load–deflection response of the middle tie beam gave a global bending modulus of approximately 10.0 GPa. In the narrow-cut model, rigid eccentric links connect the 2 mm reduced-height segment to the tie-beam axis (Fig. 3a).

The segment uses the bilinear Isotropic Nonlinear Elastic 1D relation, with an initial linear branch of modulus E = 10000 MPa and a second linear branch of tangent modulus E_p = 4 MPa beyond the tensile/compressive transitions of 11/20 MPa. The initial modulus uses this member-level value; it was not measured separately in the reduced segment. The shear modulus of 630 MPa was assigned in the RFEM material definition and was not measured in the bending

tests. The transition stresses and low second-branch tangent modulus specify the bilinear idealization; they were not determined from the member bending tests. For a linear rotational spring, the bending moment M is related to the relative rotation Δφ. Eq. 1 defines the linear spring used in the reduced representation; it is not a measured moment–rotation law:

$$M = k\,\Delta\varphi \quad (1)$$

where: k is the rotational stiffness in kNm/rad.

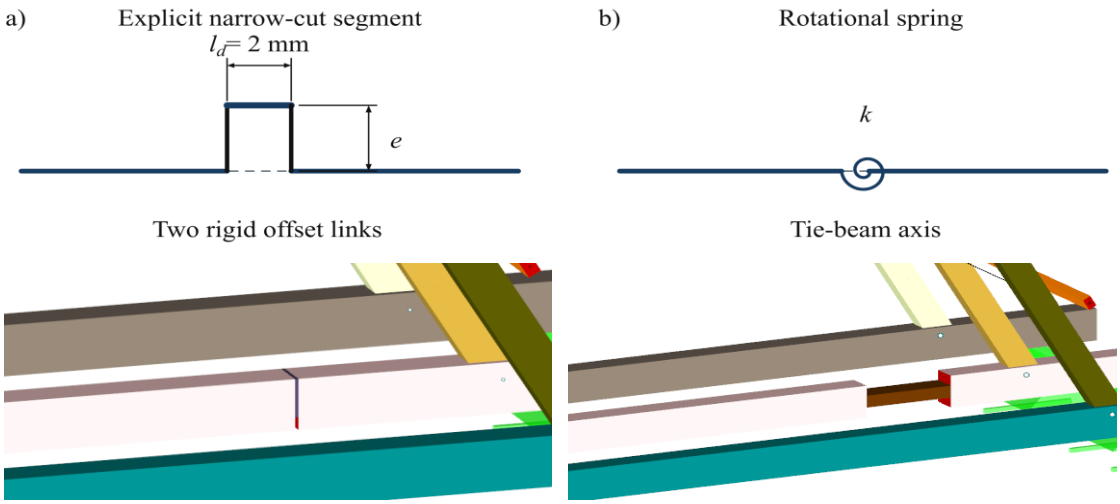


Fig. 3: Local models of tie-beam weakening. Upper: (a) eccentric 2 mm reduced-section segment with rigid links; (b) rotational spring (schematics, not to scale). Lower: RFEM views of the 2 mm segment (left) and the 200 mm long segment with a remaining height of 40 mm (right).

The reduced-height segment retains the geometry of the weakening explicitly, whereas the rotational spring condenses the bending compliance into one parameter at the weakening location. Moving from the segment representation to the spring changes how the damaged region is represented within the assembled roof model. Its consequence is examined through the displacement response.

Measured and calculated narrow cut displacements

Photogrammetry and laser scanning document heritage structures and timber roof geometry (Remondino 2011, Özkan et al. 2022); static bending provides elastic-modulus input (Ross 2015). Photogrammetric practice (Luhmann et al. 2014) supports structural displacement monitoring (Hu et al. 2021), timber-column monitoring (Li et al. 2022) and joint assessment (Kunecký et al. 2015). Their reported accuracies are not adopted here. Measured local displacement u_{cut} is the mean displacement magnitude of optical targets ID_98 and ID_99 beside the cut, relative to unloaded measurement 1. This optical quantity is a displacement magnitude rather than a signed component. Measured u_{mid} is the vertical I5V reading. Numerical u_{cut} and u_{mid} are vertical displacements at the midpoint of the reduced segment and at the tie-beam midspan, resp. Eq. 2 defines scalar increments from the fully loaded intact state, not magnitudes of vector changes between cut stages. For q ∈ {cut, mid} and x ∈ {exp, num}:

$$\Delta u_q^x(a) = u_q^x(a) - u_q^x(0) \quad (2)$$

Displacement increments retain their reported precision, including small differences from subtraction of displayed values. Fully loaded intact displacements are 7.450/11.638 mm locally/at midspan for the measurements and 7.148/10.970 mm for the explicit model. Adjusted measured displacements add the measured increments to the intact numerical displacements:

$$u_{q,1}^{ref}(a) = u_q^{num}(0) + \Delta u_q^{exp}(a) \quad (3)$$

Eq. 3 gives adjusted measured narrow-cut displacements $u_{q,1}{}^{ref}$; $u_{q,2}{}^{ref}$ are calculated narrow-cut displacements of the explicit segment model. Their assigned rotational stiffnesses are k_1 and k_2, respectively. Indices identify series, not locations. The spring-model intact displacements are 7.131/10.965 mm. Eq. 3 aligns the intact-state origins while retaining measured increments; it does not correct the cutting response.

Equivalent narrow cut depth from displacement comparison

The 20 cases in Tab. 4 combine l_d = 2, 100, 200 or 300 mm with h_r = 20–60 mm in an 80 mm high tie beam. The 200/40 mm geometry is shown in Fig. 3 (lower right). The 15 longer reductions use reduced-height segments in the same three-frame roof model, with the same bilinear relation and material inputs in Tab. 1. Their segment eccentricities, end-link definitions and solver settings are not specified. The five 2 mm cases form a separate series: its 2 mm/60 mm local value is 7.3 mm, whereas the detailed 2 cm narrow-cut value is 7.173 mm. The separate series does not redefine the calculated narrow-cut curve.

For each 100–300 mm reduction, horizontal projection from each calculated displacement to its narrow-cut curve, followed by projection onto the depth axis, gives a separate equivalent-depth reading. The adopted depth a_{eq} is an approximate common graphical assignment listed in Tab. 4. The separate in-range readings calculated with Eq. 4 assess how closely one depth represents both responses. At the adopted depth, vertical projection to the stiffness plots gives approximate graphical readings of k_1 and k_2. The logarithmic axis accommodates the large stiffness range; the connecting lines serve as visual guides. The same depth is used to read the adjusted measured displacements. For the worked example, the spring-model displacements are compared directly with those of the explicit reduced section.

Let $C_q(a)$ be the piecewise-linear calculated narrow-cut curve and $u_q{}^g$ the calculated reduced-section displacement. Linear interpolation between adjacent narrow-cut points bracketing $u_q{}^g$ gives:

$$a_q^{read} = a_i + (a_{i+1} - a_i)\,\frac{u_q^g - C_q(a_i)}{C_q(a_{i+1}) - C_q(a_i)} \quad (4)$$

Eq. 4 supplies separate in-range readings; different depths indicate that one depth cannot reproduce both piecewise-linear narrow-cut responses exactly. Readings outside the response range are left undefined. At the adopted depth, response differences are defined by $d_q = C_q(a_{eq}) - u_q{}^g$ (Tab. 4). They measure displacement agreement, not spring-model error or a statistical uncertainty interval. The additional decimal places reflect interpolation of rounded input values.

RESULTS AND DISCUSSION

Narrow cut displacements and equivalent rotational stiffness

Measured increments increase more strongly than those of the numerical narrow-cut representation (Fig. 4). At 7 cm, the measured increments are 14.839 mm locally and 6.188 mm at midspan, compared with numerical increments of 8.928 and 2.622 mm. The measured and calculated displacement series are therefore kept separate. The shapes of the curves also influence the graphical reading. Between 2 and 4 cm, the calculated displacement increments remain small; the increase is much larger between 4 and 6 cm. A displacement ordinate must therefore be interpreted within the interval that brackets it. The same change in displacement does not imply the same change in equivalent depth throughout the curve.

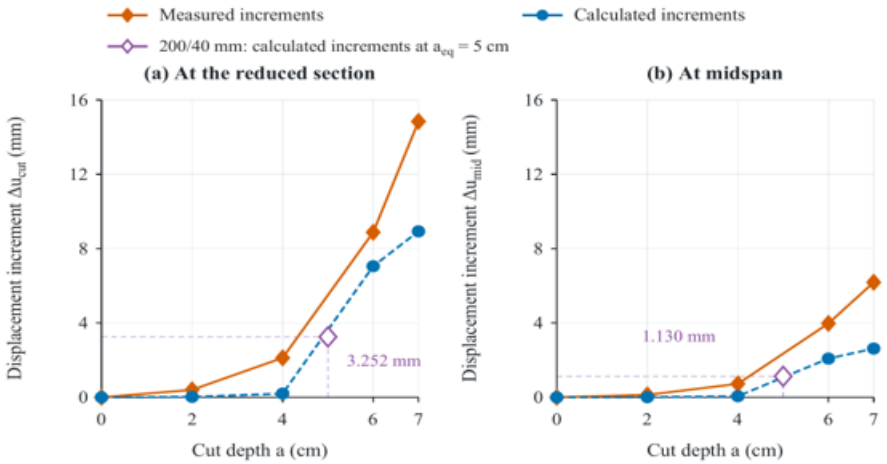


Fig. 4: Measured and calculated narrow-cut displacement increments: (a) local; (b) midspan. Each uses its own intact state. Open purple markers show the 200/40 mm calculated increments at the adopted equivalent depth.

Both rotational stiffness series decrease with cut depth, with k_1 lower than k_2 at all four measured depths (Tab. 2). At 7 cm, k_1 is 0.001 kNm/rad and k_2 is 2.4 kNm/rad. The small k_1 value describes a near-hinge approximation; the 7 cm cut remains a connected section.

Tab. 2: Narrow-cut displacements in mm and assigned rotational stiffnesses in kNm/rad.

a [cm]	Measured (adj.) $u_{cut,1}^{ref}$	Measured (adj.) $u_{mid,1}^{ref}$	Calculated $u_{cut,2}^{ref}$	Calculated $u_{mid,2}^{ref}$	k_1	k_2
0	7.148	10.970	7.148	10.970	–	–
2	7.549	11.101	7.173	10.978	200	700
4	9.269	11.695	7.349	11.030	34	400
6	16.025	14.945	14.201	13.054	2.5	5.1
7	21.987	17.158	16.076	13.592	0.001	2.4

Note: Narrow-cut stiffnesses were reported previously (Brodniansky et al. 2026b). Measured displacements are adjusted using Eq. (3); the intact state has no assigned spring stiffness.

At 6 cm, the k_1 difference is −0.007 mm locally but −1.097 mm at midspan; at 7 cm, the differences are −3.081 and −2.364 mm. Thus the k_1 assignments do not reproduce both adjusted measured displacements closely at deep cuts. At 7 cm, k_2 differences are +0.030/+0.285 mm (Tab. 3), supporting consistency with the calculated narrow-cut

displacements; these values do not establish experimental equivalence.

Tab. 3: Narrow-cut spring-model displacements and differences from the corresponding displacement series in Tab. 2; all values in mm.

Assignment	a [cm]	Spring u_{cut}	Spring u_{mid}	Difference u_{cut}	Difference u_{mid}
k_1	2	7.573	11.107	0.024	0.006
k_1	4	9.324	11.673	0.055	-0.022
k_1	6	16.018	13.848	-0.007	-1.097
k_1	7	18.906	14.794	-3.081	-2.364
k_2	2	7.260	11.006	0.087	0.028
k_2	4	7.356	11.037	0.007	0.007
k_2	6	14.221	13.262	0.020	0.208
k_2	7	16.106	13.877	0.030	0.285

Note: Difference = spring-model displacement minus the corresponding Tab. 2 value: adjusted measured for k_1, calculated for k_2.

Liu and Xiong (2018) tested the moment–rotation response of bolted timber connections separately from the lateral response of timber portal frames. The spring stiffnesses in the present study were assigned from displacement responses without separate moment–rotation measurements. At the 6 cm cut, the spring assigned from the adjusted measured series agrees closely with the local displacement but less closely with the midspan deflection (Tab. 3). Agreement at the cut is therefore insufficient to establish agreement at midspan.

Influence of reduced section length and remaining height

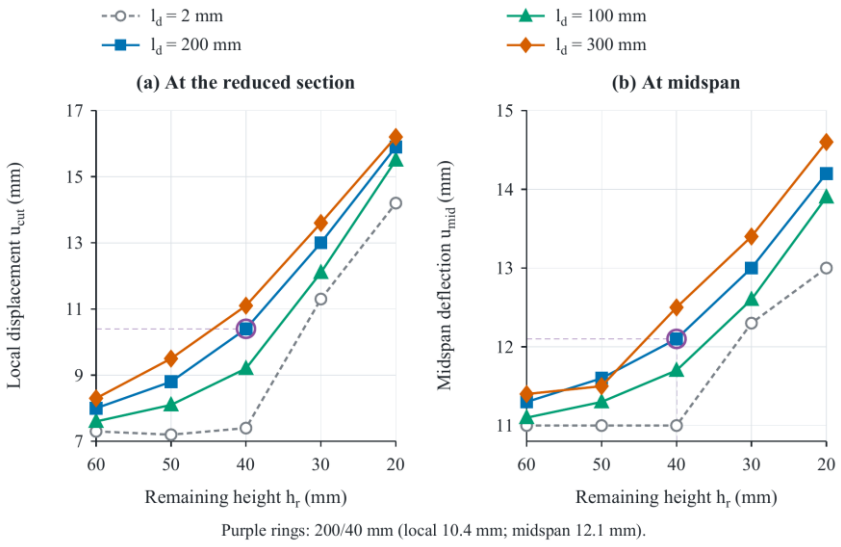


Fig. 5: Calculated reduced-section displacements: (a) local; (b) midspan. Purple rings mark 200/40 mm. Remaining height decreases from left to right; the 2 mm series is separate.

The calculated series in Fig. 5 show how the extent of the weakened region affects both displacements. At h_r = 40 mm, lengths of 100, 200 and 300 mm give local/midspan pairs of 9.2/11.7, 10.4/12.1 and 11.1/12.5 mm. The local response changes more across this length range than the midspan deflection. Identical remaining heights alone do not determine the assignment, because reduction length also affects the calculated response.

Across the five remaining heights, local displacement increases with length in every row.

Midspan deflection follows that order in four rows; at h_r = 50 mm, the 100/200/300 mm values are 11.3/11.6/11.5 mm. This small reversal is retained in the comparison. The two plots therefore describe related but distinct responses, and a length trend inferred from the local quantity alone does not fully describe the global result. For each of the three longer reduction lengths, decreasing the remaining height increases both displacements. For both quantities, the largest increase between adjacent height levels occurs from 30 to 20 mm. The matrix allows the effects of reduction length and remaining height to be examined separately.

Tab. 4: Calculated reduced-section displacements, adopted depths and stiffnesses, and differences from calculated narrow-cut displacements at the adopted depth.

l_d [mm]	h_r [mm]	u_{cut}^{num} [mm]	u_{mid}^{num} [mm]	a_{eq} [cm]	k_1 [kNm/rad]	k_2 [kNm/rad]	d_{cut} [mm]	d_{mid} [mm]
2	60	7.3	11	2	200	700	–	–
2	50	7.2	11	2.5	140	600	–	–
2	40	7.4	11	4	34	400	–	–
2	30	11.3	12.3	5.3	6	23	–	–
2	20	14.2	13	6	2.5	5.1	–	–
100	60	7.6	11.1	4.1	30	300	+0.092	+0.031
100	50	8.1	11.3	4.2	22	240	-0.066	-0.068
100	40	9.2	11.7	4.6	15	100	+0.205	-0.063
100	30	12.1	12.6	5.5	5	10	+0.388	-0.052
100	20	15.5	13.9	6.8*	0.004	3	+0.201	-0.416
200	60	8	11.3	4.2	22	240	+0.034	-0.068
200	50	8.8	11.6	4.5	19	140	+0.262	-0.064
200	40	10.4	12.1	5	9	40	+0.375	-0.058
200	30	13	13	5.8	4	8	+0.516	-0.148
200	20	15.9	14.2	7*	0.001	2.4	+0.176	-0.608
300	60	8.3	11.4	4.2	22	210	-0.266	-0.168
300	50	9.5	11.5	4.6	15	100	-0.095	+0.137
300	40	11.1	12.5	5.3	6	20	+0.703	-0.154
300	30	13.6	13.4	6.1	1	4	+0.789	-0.292
300	20	16.2	14.6	7*	0.001	2.4	-0.124	-1.008

Note: $d_q = C_q(a_{eq}) - u_q^g$. * At least one displacement exceeds its calculated range, so an in-range depth cannot be read for both displacements. Dashes refer to the separate 2 mm series.

Graphical determination of equivalent depth and stiffness

The 200/40 mm example follows the full graphical sequence in Fig. 6. The 200 mm long segment retains a height of 40 mm from the original 80 mm tie beam; its RFEM geometry appears in Fig. 3. The calculated local displacement of 10.4 mm enters panel (a), and the midspan deflection of 12.1 mm enters panel (b). Separate intersections with the calculated narrow-cut curves give depths of 4.89 and 5.06 cm (Eq. 4). Their difference of approximately 0.17 cm shows the closeness of the two readings. The approximate graphical assignment of 5.0 cm lies between them.

Panel (c) uses that adopted depth to read the approximate rotational stiffnesses k_1 = 9 and k_2 = 40 kNm/rad. At 5.0 cm, the calculated narrow-cut curves give 10.775/12.042 mm, hence d_{cut} = +0.375 mm and d_{mid} = −0.058 mm relative to the longer reduction. The signs indicate that the narrow-cut curve gives a larger local displacement and a slightly smaller midspan deflection.

The corresponding pair of approximately 12.8/13.4 mm is read from the adjusted measured curves at 5.0 cm; it was not measured for the 200 mm reduction. The subsequent k_2 spring-model pair is 9.0/11.6 mm, differing by −1.4/−0.5 mm from the explicit reduction. This

comparison concerns the actual response of the replacement model, whereas the preceding differences concern the narrow-cut curves used to assign its stiffness.

Comparison from each model's own intact state leads to the same finding. Local/midspan increments are 3.252/1.130 mm for the explicit reduction and 1.869/0.635 mm for the spring model, about 57%/56% of the former. The smaller spring response therefore persists after the initial displacement levels are removed.

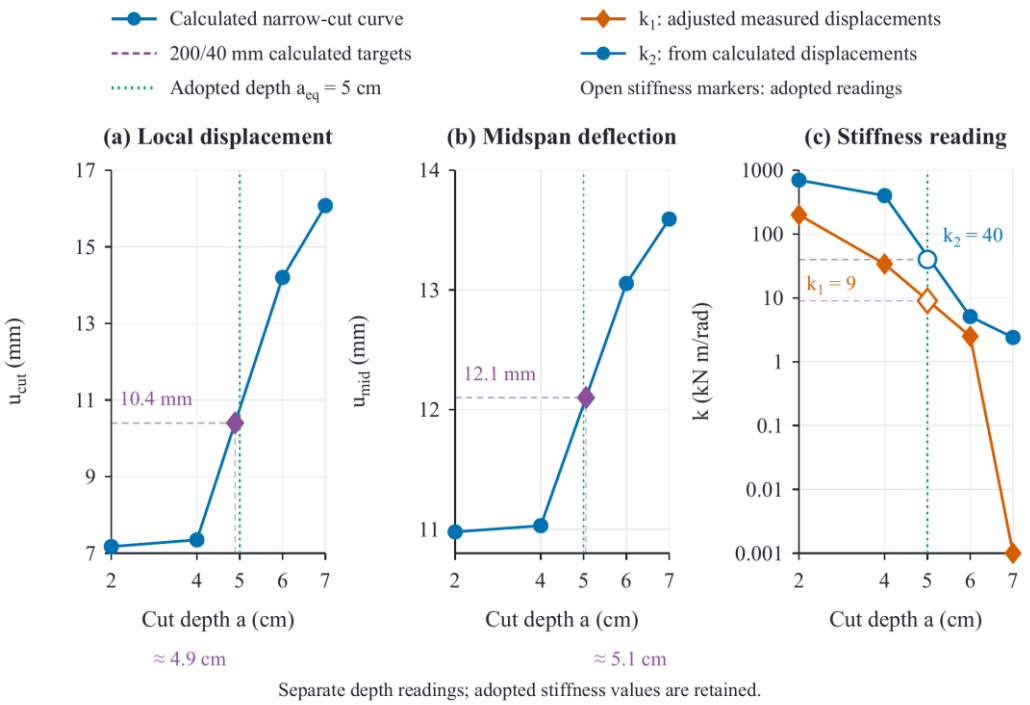


Fig. 6: Graphical assignment for 200/40 mm: (a,b) separate depth readings of 4.9/5.1 cm; (c) adopted k_1 = 9 and k_2 = 40 kNm/rad at a_{eq} = 5 cm. Open stiffness markers denote graphical readings; lines guide the eye.

Equivalent cut depths and agreement of the two displacements

At h_r = 40 mm, lengths 100/200/300 mm have a_{eq} = 4.6/5.0/5.3 cm, k_1 = 15/9/6 and k_2 = 100/40/20 kNm/rad (Tab. 4; Fig. 7). The tabulated depth alone does not uniquely recover the graphical stiffness assignment: the 200/60 and 300/60 mm cases both give a_{eq} = 4.2 cm but k_2 = 240 and 210 kNm/rad. The separate 2 mm cases with h_r = 50/30 mm retain depths of 2.5/5.3 cm rather than the geometrical 3/5 cm. The influence of reduction length on the adopted depth depends on the remaining height. In Fig. 7a, the depth markers for the 100–300 mm reductions cluster more closely at a remaining height of 60 mm than at 30 or 40 mm.

Shojo et al. (2009) related the rotational stiffness of a timber member with partial section loss to the length and flexural rigidity of the reduced region in bending tests. Murphy (1986) observed a greater increase in deflection for a rectangular notch than for a saw slit of the same relative depth in glulam beams and represented the deflection using a reduced second moment of area over an effective notch length. In the present roof model, the decrease in the assigned stiffnesses with increasing length at a remaining height of 40 mm (Tab. 4) is consistent with the relevance of the affected length. The member tests provide a qualitative comparison:

the present assignments also reflect the assembled roof and the combined tension and bending in the tie beam.

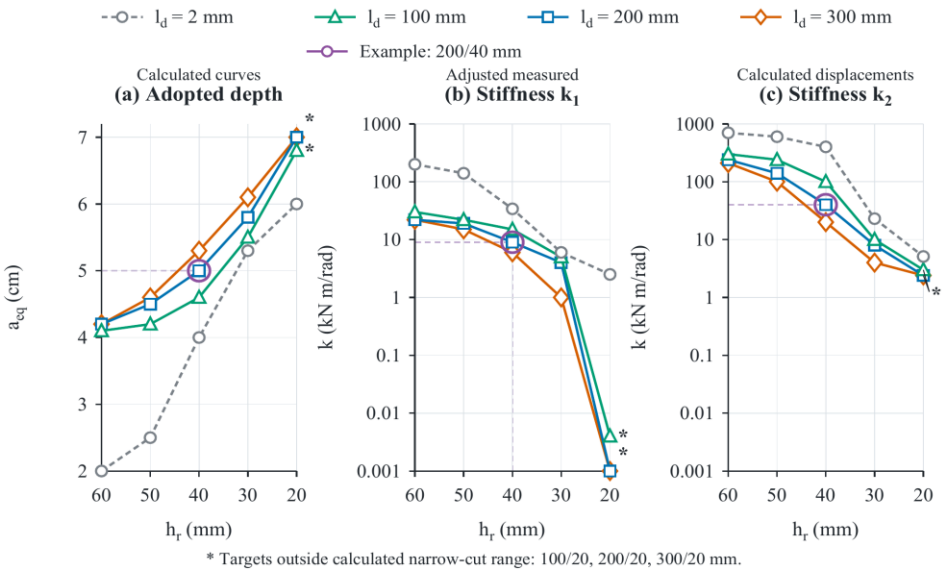


*Fig. 7: Adopted (a) equivalent depths, (b) k_1 from adjusted measured displacements and (c) k_2 from calculated displacements. Series colours denote reduction length; purple rings mark 200/40 mm. * Out-of-range targets: 100/20, 200/20 and 300/20 mm. The 200/20 and 300/20 markers coincide. Lines guide the eye.*

Fig. 8 plots midspan deflection against local displacement. The calculated narrow-cut curve joins the response pairs obtained at successive cut depths. A longer-reduction point on this curve would permit one equivalent depth to represent both quantities; separation from the curve shows why one depth cannot match both responses exactly.

Both targets permit inverse interpolation for 12 of the 15 longer cases. At 300/30 mm, the separate depths of 5.82/6.64 cm differ by 0.82 cm; the adopted depth of 6.1 cm gives d_{cut} = +0.789 mm and d_{mid} = −0.292 mm (Tab. 4). Compared with the worked example, this case shows a wider separation between the two readings. The depth gap compares the two inverse readings; the signed differences quantify the displacement discrepancies remaining at the adopted depth.

At h_r = 20 mm, the 100/200 mm cases exceed the calculated midspan maximum of 13.592 mm; the 300 mm case also exceeds the local maximum of 16.076 mm. Their marked assignments remain tabulated. At 300/20 mm, a_{eq} = 7 cm gives differences of −0.124/−1.008 mm, while both inverse readings remain outside range.

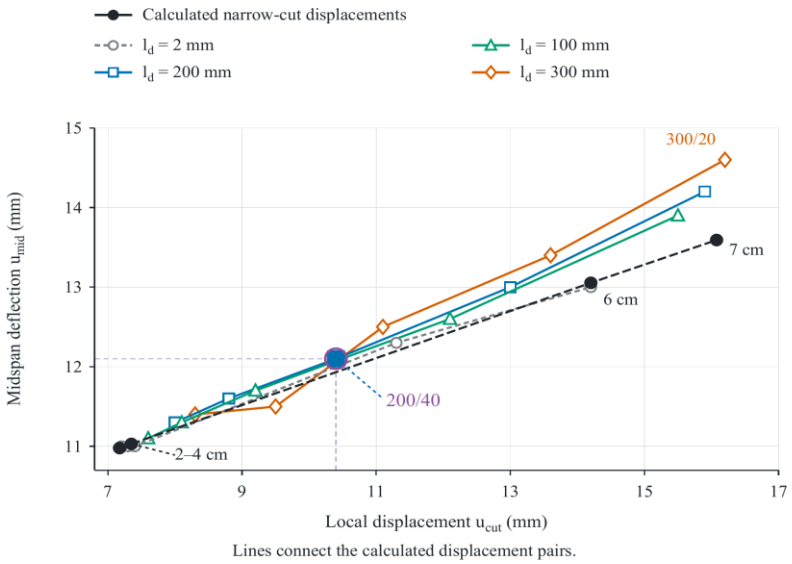


Fig. 8: Midspan deflection against local displacement; the purple ring marks 200/40 mm. Reduced-section pairs need not lie on the calculated narrow-cut curve. Lines connect reported points.

Recorded deflection during cutting

For consistent optical–inductive comparison, the previously reported 7 cm I5V reading of 18.900 mm (Brodniansky et al. 2026a,b) is corrected to 17.825 mm from the near-constant level at 1300 s (Fig. 9). The increment 17.825 − 11.6375 = 6.1875 mm rounds to 6.188 mm in Eq. 3. This updates measured midspan comparisons; the calculated narrow-cut curves, equivalent-depth procedure and 200/40 mm example remain unchanged. Selected times in the 0.5 s record identify responses, not cutting onsets; intermediate depths are unassigned. Each stage has one optical acquisition (Tab. 5).

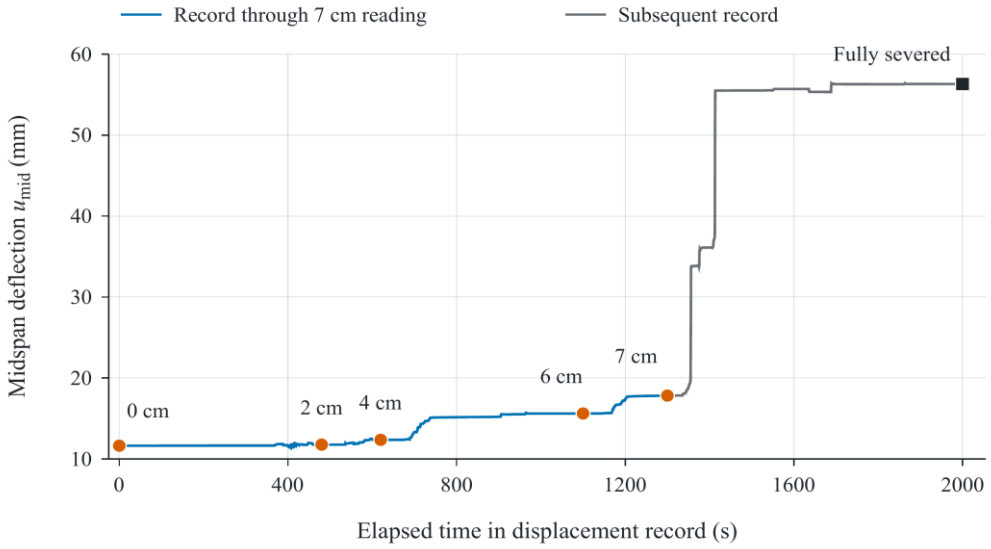


Fig. 9: Recorded I5V midspan deflection. Circles mark selected 0–7 cm readings; the square marks the fully severed state at 2000 s, shown for context. Lines include intervening readings.

Tab. 5: Midspan increments of the middle tie beam relative to measurement 19; values in mm.

Cut depth [cm]	Optical ID_66	Optical ID_26	Inductive I5V	Difference ID_66 − I5V	Difference ID_26 − I5V
0	0.000	0.000	0.000	0.000	0.000
2	0.180	0.139	0.131	+0.049	+0.008
4	0.842	0.708	0.725	+0.117	−0.017
6	3.820	3.436	3.975	−0.155	−0.539
7	6.666	6.055	6.188	+0.478	−0.132

Note: Optical values are magnitudes of coordinate changes at opposite midspan faces; I5V is the vertical deflection increment. Difference = optical − I5V, calculated before rounding.

Interpretation and scope of the demonstration

The geometric reduction depth and equivalent cut depth describe different quantities. The 200/40 mm segment has a geometric height loss of 40 mm, while its adopted narrow-cut depth is 50 mm. The equivalent depth expresses the association obtained from response curves. Its purpose is to describe the longer reduction in terms of the narrow-cut series; the specified segment length and remaining height remain the geometric inputs. The demonstration is confined to the tested roof segment, member dimensions and ballast arrangement. Only narrow cuts were tested experimentally; longer reductions are numerical cases. Equivalent depths and stiffnesses apply to this configuration and are not transferable to members of other dimensions or roof arrangements. The single linear spring represents rotational compliance at the studied response state. Compatibility of displacement curves does not verify local stresses, axial compliance, contact, strength, failure or load-history equivalence with the bilinear segment. Complete severing and propagated measurement/model uncertainty are outside the analysis.

CONCLUSIONS

The graphical procedure connects the geometry of finite-length weakening with narrow-cut displacement curves and assigned rotational stiffnesses. The 15 cases show that both length and remaining height affect the association. Local displacement and midspan deflection provide complementary checks, so the assignment can be traced through the graphs rather than inferred from section height alone. For the 200/40 mm example, local and midspan equivalent-depth readings are 4.89 and 5.06 cm, with an adopted graphical depth of 5.0 cm. Calculated narrow-cut curves differ from the explicit reduced-section response by +0.375 mm locally and −0.058 mm at midspan. The corresponding differences for the subsequent k_2 spring model are −1.4 and −0.5 mm. For deeper narrow cuts, the k_1 spring model does not closely reproduce both adjusted measured displacements. Both displacement quantities yield in-range equivalent depths for 12 of the 15 longer reductions; three exceed a calculated response range. The largest in-range difference between the two depth readings is 0.82 cm. The procedure provides an approximate graphical association for the studied roof segment.

ACKNOWLEDGMENTS

The research was supported by the project “Wooden structures prevention and maintenance for heritage conservation purposes” (NAKI III, reg. No. DH23P03OVV005), provided by the Ministry of Culture of the Czech Republic.

REFERENCES

1. Branco, J.M., Descamps, T., 2015: Analysis and strengthening of carpentry joints. Construction and Building Materials 97: 34–47.
2. Brodniansky, J., Martinkovičová, S., Sandanus, J., Klas, T., Kunecký, J., Bláha, J., Kloiber, M., 2026a: The experimental investigation of a model of a historical-type timber roof segment under progressive tie-beam weakening. Wood Research 71(2): 331–346.
3. Brodniansky, J., Martinkovičová, S., Sandanus, J., Klas, T., Kunecký, J., Bláha, J., Kloiber, M., 2026b: Experimental investigation of load redistribution in a historic-type timber roof segment under progressive tie-beam weakening. Wood Research 71(3): 437–450.
4. Cruz, H., Yeomans, D., Tsakanika, E., Macchioni, N., Jorissen, A., Touza, M., Mannucci, M., Lourenço, P.B., 2015: Guidelines for on-site assessment of historic timber structures. International Journal of Architectural Heritage 9(3): 277–289.
5. Dietsch, P., 2011: Robustness of large-span timber roof structures. Structural aspects. Engineering Structures 33(11): 3106–3112.
6. Hu, J., Liu, E., Yu, J., 2021: Application of structural deformation monitoring based on close-range photogrammetry technology. Advances in Civil Engineering 2021: 6621440.
7. Kunecký, J., Sebera, V., Hasníková, H., Arciszewska-Kędzior, A., Tippner, J., Kloiber, M., 2015: Experimental assessment of a full-scale lap scarf timber joint accompanied by a finite element analysis and digital image correlation. Construction and Building Materials 76: 24–33.
8. Li, H., Dai, Y., Qiu, H., He, X., 2022: Application of multi-camera digital image correlation in the stability study of the long timber column with the circular cross-section under axial compression. BioResources 17(1): 1717–1728.
9. Liu, Y., Xiong, H., 2018: Lateral performance of a semi-rigid timber frame structure: theoretical analysis and experimental study. Journal of Wood Science 64(5): 591–600.
10. Luhmann, T., Robson, S., Kyle, S., Boehm, J., 2014: Close-range photogrammetry and 3D imaging. 2nd ed. De Gruyter, Berlin/Boston.
11. Lyu, M., Zhu, X., Yang, Q., 2017: Connection stiffness identification of historic timber buildings using temperature-based sensitivity analysis. Engineering Structures 131: 180–191.
12. Martinkovičová, S., Sandanus, J., Brodniansky, J., Ondrašinová, L., 2025: Static analysis of selected types of roof trusses considering the weakening of the structural elements. Slovak Journal of Civil Engineering 33(3): 47–53.
13. Moya, R., Tenorio, C., 2017: Strength and displacement under tension and compression of wood joints fastened with nails and screws for use in trusses in Costa Rica. Wood Research 62(1): 139–156.
14. Munafò, P., Stazi, F., Tassi, C., Davì, F., 2015: Experimentation on historic timber trusses to identify repair techniques compliant with the original structural–constructive conception. Construction and Building Materials 87: 54–66.
15. Munch-Andersen, J., Dietsch, P., 2011: Robustness of large-span timber roof structures—Two examples. Engineering Structures 33(11): 3113–3117.
16. Murphy, J.F., 1986: Strength and stiffness reduction of large notched beams. Journal of Structural Engineering 112(9): 1989–2000.

17. Neusch, M., Sandanus, J., Freudenberger, K., 2022: Experimental verification of the modern semi-rigid timber connections. Wood Research 67(6): 1005–1016.
18. Özkan, T., Pfeifer, N., Styhler-Aydın, G., Hochreiner, G., Herbig, U., Döring-Williams, M., 2022: Historic timber roof structure reconstruction through automated analysis of point clouds. Journal of Imaging 8(1): 10.
19. Remondino, F., 2011: Heritage recording and 3D modeling with photogrammetry and 3D scanning. Remote Sensing 3(6): 1104–1138.
20. Ross, R.J. (ed.), 2015: Nondestructive evaluation of wood: Second edition. General technical report FPL-GTR-238. Madison, WI: U.S. Department of Agriculture, Forest Service, Forest Products Laboratory.
21. Shojo, N., Hayasaki, Y., Ohashi, Y., 2009: Study on flexural performance of wooden members with the partial loss of sectional area. Journal of Structural and Construction Engineering 74(635): 97–103.
22. Sørensen, J.D., 2011: Framework for robustness assessment of timber structures. Engineering Structures 33(11): 3087–3092.
23. Stitic, A., Nguyen, A.C., Rezaei Rad, A., Weinand, Y., 2019: Numerical simulation of the semi-rigid behaviour of integrally attached timber folded surface structures. Buildings 9(2): 55.
24. Xiao, F., Zhu, W., Meng, X., Chen, G.S., 2022: Parameter identification of structures with different connections using static responses. Applied Sciences 12(12): 5896.
25. Yang, X., Zhao, Q., Hao, D., Wang, J., Fu, S., Ma, L., 2020: Flexural behavior of OSB reinforced wood truss. Wood Research 65(2): 245–256.
26. Yeomans, D., 2003: The repair of historic timber structures. London: Thomas Telford.
27. Zybała, T., Szepietowska, K., Bukal, G., Lubowiecka, I., 2022: Portico farmhouses of the Vistula Delta: architecture, current state and finite element modelling of timber roof truss under material and cross-section uncertainty. International Journal of Architectural Heritage 16(12): 1885–1906.

JÁN BRODNIANSKY*, SILVIA BRODNIANSKY,
JAROSLAV SANDANUS, TOMÁŠ KLAS
SLOVAK UNIVERSITY OF TECHNOLOGY IN BRATISLAVA
DEPARTMENT OF STEEL AND TIMBER STRUCTURES
RADLINSKÉHO 11, 810 05 BRATISLAVA
SLOVAK REPUBLIC
*Corresponding author: jan_brodniansky@stuba.sk

JIŘÍ KUNECKÝ, JIŘÍ BLÁHA, MICHAL KLOIBER
INSTITUTE OF THEORETICAL AND APPLIED MECHANICS
CZECH ACADEMY OF SCIENCES
PROSECKÁ 809/76, 190 00 PRAGUE 9
CZECH REPUBLIC